

# Verticalized-Tip Trajectory Tracking of a 3D-Printable Soft Continuum Robot: Enabling Surgical Blood Suction Automation

Jiewen Lai<sup>1</sup>, Student Member, IEEE, Kaicheng Huang<sup>2</sup>, Bo Lu<sup>3</sup>, Qingxiang Zhao<sup>4</sup>, and Henry K. Chu<sup>5</sup>, Member, IEEE

**Abstract**—Soft-bodied robotic manipulators have great potential for use in minimally invasive surgery, owing to their advantages of high flexibility with infinite degrees of freedom (DOF). One of the potential applications is to perform blood suctioning, which is inevitable during the surgery. To attain higher efficiency in suctioning, the robotic tip should remain vertical while moving along on the work surface. Motivated by this application, this article presents a novel soft robot design and its control scheme to properly configure the tip of a two-segment soft robot while following a planned trajectory on the work surface. Aiming to reduce the incision size and the possibility of infection, a 3D-printed soft-bodied manipulator utilizing the cable-driven mechanism with a diameter of 9 mm was designed and fabricated. An additional DOF was added through a motorized insertion stage. The robot system was modeled using piecewise constant-curvature assumption, and an RGB-D vision was employed to enhance the accuracy of the kinematic-based controller. Performances of the tip positioning and verticalizing were evaluated via simulation, and further verified through experiments. The results confirm that the manipulator is capable of following different trajectories at various velocities while keeping its tip vertical. Compared to other similar works, our results are satisfactory with an root-mean-square error of trajectory tracking within 7 mm, and a maximum angular deviation of 6°. Fluid suction experiments were conducted to demonstrate its effectiveness for automated 3-D suction. This article offers a new tool to support the surgeons for surgical blood suction.

**Index Terms**—Soft robot, surgical robot, trajectory tracking.

Manuscript received January 8, 2021; revised March 26, 2021 and May 27, 2021; accepted June 10, 2021. Date of publication June 22, 2021; date of current version June 16, 2022. Recommended by Technical Editor J. A. Schultz and Senior Editor G. Alici. This work was supported in part by the HK PolyU under Grants 4-RKCM and G-UAFR. (Corresponding author: Henry K. Chu.)

Jiewen Lai, Kaicheng Huang, Qingxiang Zhao, and Henry K. Chu are with the Department of Mechanical Engineering, The Hong Kong Polytechnic University, Hong Kong (e-mail: jw.lai@connect.polyu.hk; huangkc@sustech.edu.cn; qingxiang.zhao@connect.polyu.hk; henry.chu@polyu.edu.hk).

Bo Lu is with the CUHK T Stone Robotics Institute, The Chinese University of Hong Kong, Hong Kong (e-mail: bolu@cuhk.edu.hk).

This article has supplementary material provided by the authors and color versions of one or more figures available at <https://doi.org/10.1109/TMECH.2021.3090838>.

Digital Object Identifier 10.1109/TMECH.2021.3090838

## I. INTRODUCTION

SOFT continuum manipulators are constructed from highly compliant soft materials that enable continuous elastic deformation to induce different motions [1]. These manipulators are getting more attention because of their capability of interacting with humans safely. In general, soft robots can be characterized as dexterous robotic manipulators with theoretically infinite degrees of freedom (DOF). The high compliance and low Young's modulus of soft material make soft manipulator become a promising robotic instrument to interact with human anatomy, especially in robot-assisted minimally invasive surgeries (MIS) [2]. During MIS, the surgeon has limited accessibility to refrain from the blood vessels, and that limitation certainly presents a risk of major bleeding in the surgical site. Pulsatile bleeding often has a serious impact on the endoscopic vision, including brightness and sharpness [3]. After conducting hemostasis, the residual blood shall be evacuated timely so that the surgery can be continued. In robot-assisted MIS, most of the sophisticated procedures are ought to be manually manipulated by well-trained surgeons [4]. However, some standardized tasks, such as surgical wound suturing [5], biopsy [6], and surgical blood suction, can be fully robotized and automated so that the surgeon can concentrate on other difficult tasks. Fluid residual suction and saline irrigation are usually the main two procedures for surgical site cleaning. To the best of authors' knowledge, the blood suctioning procedure has not yet been robotized in the current stage, and it requires a bedside assistant to manually operate an aspirator tube to clear the surgical site [3], [7]. The efficiency of surgical blood suction can be improved by introducing a dexterous soft robotic manipulator as blood aspirator. With the limited accessibility to the intracavity, where the incision ports are usually around 5–15 mm [8], a miniaturized soft continuum manipulator would be an ideal surgical tool for the automated suction tasks.

In this proof-of-concept work, we present a soft robot prototype for use in surgical blood suction. Several considerations are taken in designing and controlling the robot, including the following:

- 1) The pointing direction of the manipulator's tip should always be vertical to the fluid level while moving over a large surface for tractorized blood suction task.

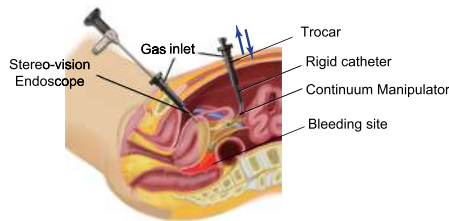


Fig. 1. Schematic of concept: a soft continuum robot for blood suction in the laparoscopic (minimally invasive) surgery.

- 2) The motion at the surgical port as the remote-center-of-motion (RCM) is limited to insertion–retraction only (tube feeding) to minimize possible interference between the robot and the patient.
- 3) The soft body can be easily detached for disposal after each operation to eliminate the risk of infection.

The aforementioned key-points are briefly illustrated by a schematic in Fig. 1.

### A. Related Work

End-effector trajectory tracking is essential to the automation of a soft manipulator. In view of the model complexity due to the material elasticity, some researchers incorporate the model-free method, such as machine learning, to estimate the motion behavior of a soft robot. Lee *et al.* [9] proposed a nonparametric online learning approach to control a single segment soft fluid-driven continuum robot by learning the inverse kinematics (IK) directly using the electromagnetic (EM) tracked data and the actuation data. Giorelli *et al.* [10] utilized a feedforward neural network to solve the IK of a cable-driven soft arm with a nonconstant curvature deformation. Learning the motion behavior of the soft robot using different models [11], [12], or different on-board sensors [13], [14], had been investigated. However, these learning approaches usually require rich data for computationally expensive training, and the pretrained model would be only applicable to that particular prototype. Yip and Camarillo [15] proposed a model-free closed-loop controller to manipulate a 2-D continuum robot in a constraint environment based on the online optimization of the Jacobian matrix. Force feedback from the tendons was also incorporated in the control. Visual servoing is another model-free approach that enables the soft robot to conduct trajectory tracking [16]–[19] based on real-time sensory feedback to minimize the error between the current and desired values.

Several model-based control schemes for end-effector positioning have also been studied. In [20], a dynamic model was developed using the Newton–Euler model for the trajectory tracking of a flexible manipulator in 2-D. Kato *et al.* [21] modeled a multicell backbone continuum robot based on bending propagation from each cell and derived the kinematics mapping from the cable tension to the robot posture offline. In other studies, a geometrically exact approach based on the Cosserat theory was employed to model the elastic body as a curve to enhance the geometric continuity of the robot to predict the 3-D [22] motions. In the field, piecewise constant-curvature

(PCC) assumption is generally adopted in modeling the deformation of a soft segment [2], [4], [11], [23]–[28]. The PCC model decomposes the robot kinematics into two mappings, i.e., from the actuator space to the configuration space, and from the configuration space to the task space. The configuration space for one soft segment is represented by an arc, which can be defined by the arc length, the arc curvature (bending angle), and the rotational angles of the arc-containing plane concerning a reference direction. Della Santina *et al.* [27] proposed an optimized PCC-based controller to conduct 3-D trajectory tracking of a soft robot tip and it was verified through simulation. Qi *et al.* [29] designed a fuzzy controller to realize 3-D tip trajectory tracking on a single-segment tendon-driven continuum robot prototype. The pneumatic STIFF-FLOP robot, which was designed for MIS and had been operated in cadaver trial, was examined with closed-loop control for one-segment [30] and two-segment bending [23]. Gong *et al.* [31] designed an underwater system with a three-segment soft manipulator for grasping seafood animals with orientation control. The merit of model-based control is that the model can be easily updated to adapt to the change in the robot parameters.

Although soft robot trajectory tracking has been studied by a number of groups, many of them were examined through a single segment robot for demonstration [9], [15]–[18], [23]. With limited controllable parameters, only the position of the end-effector was tracked but its orientation was not required nor considered in their applications. Trajectory control on two or more segments has also been reported. With the existence of multiple solutions to bring the end-effector to the desired position, one practice is to find the inputs that can minimize the position error [15]. Similarly, the robot shape or configuration was not considered. In order to bring the tip to the desired position and in vertical, additional information such as the orientation, or the intermediate point of the robot [11], [32], [33] from the current robot is also needed. In addition, it is also challenging to precisely control the end-effector of a multisegment robot, as changing the end-effector position would also lead to a change of the orientation. Unlike the rigid robot, a wrist joint cannot be installed at the end-effector of the soft robot to decouple the motion.

### B. Contributions

In this article, we aim to achieve both position and orientation control of a two-segment soft manipulator. For an inextensible segment, the parameters in the PCC model are reduced to two, having a spherical dome-like workspace [9]. To enhance the controllability of the robot, an additional translation DOF is added, giving a total of 5-DOF configuration space to enable trajectory following on a work surface with a vertical tip. To resolve the coupling effect, we propose an opposite-bending configuration to the two segments to maintain the same orientation of the tip throughout the 3-D trajectory tracking task. An RGB-D camera, mimicking a 3-D positioning system (such as stereo endoscope and EM tracker), was employed to monitor the tip and provide feedback for the model-based closed-loop control to enhance the positioning accuracy. Experiments were conducted to examine

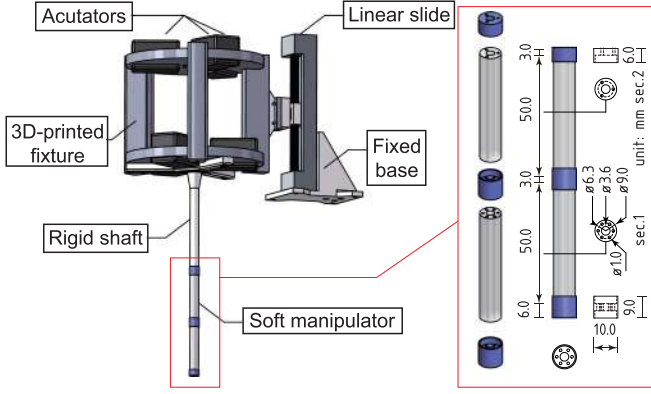


Fig. 2. Layout of the soft continuum robot and prototype assembly.

the performance in tracking different trajectories on the desired plane under different speeds.

This article contributes the following:

- 1) The design and prototyping of a miniature two-segment cable-driven 3D-printed soft robot with a hollow structure for surgical blood suction.
- 2) A controller strategy, which includes the verticalized configuration strategy, the rapid point cloud search-based IK, the RGB-D visual feedback control, and the image-based suction path generation, enables effective and automated blood suction.

## II. MANIPULATOR AND PROTOTYPE DESIGN

The design layout of the 3D-printed soft manipulator is shown in Fig. 2. The manipulator consists of two 50 mm long soft segments with a diameter of 9 mm. The distal segment (section view 2 in Fig. 2) has a  $\varnothing 3.6$  mm main channel for suction and three surrounding channels for cabling. Similarly, the proximal segment has a main channel and six surrounding channels for cabling (section view 1 in Fig. 2). The soft body of the manipulator was 3D-printed using Agilus30 (Stratasys Ltd., MN, USA), which is a durable, soft-touch rubber-like PolyJet photopolymer. The rigid disks mounted at the distal tip, proximal base, and between two segments, were 3D-printed using polylactic-acid (PLA). Cables were wired along the channels of the body, and polyethylene braided fishing lines with a diameter of 0.26 mm were selected to minimize cable elongation during stretching. The cables were fixed to the disks by tying knots. The total mass of the two soft elastomers, including the PLA disks, is approximately 5.2 g. Experiments confirm the durability of the robot prototype through hundreds of trials without any degradation or repair.

Similar to our previous study [34], each cable was driven by a Dynamixel XM430-W350 smart actuator (ROBOTIS, Seoul, Korea). But in this article, these actuators were mounted in a 3D-printed fixture, which was connected on a linear slide (stepper motor-driven lead screw with a pitch of 1 mm) to provide the insertion–retraction motion, as shown in Fig. 2. This translational platform configures an RCM mechanism [35], which is commonly used by the surgical robots to limit the allowable motion of the attached tool at the incision port. Compared to

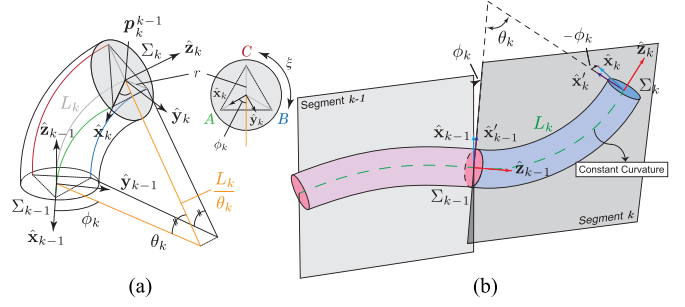


Fig. 3. (a) Geometric transformation between actuation space and configuration space for the  $k$ th segment. Three cables are isometrically distributed for actuation ( $\xi = 2\pi/3$ ). The constant distance between the centric point and the cable aperture at the section view is  $r$ . (b) Constant curvature arc parameters of a continuum manipulator model: two neighboring segments.

the state-of-the-art da VinciXi suction tool (EndoWrist Suction Irrigator), which employs a long, cylindrical rigid structure with a foldable tip, our soft-bodied device can cause less damage to nearby tissues in case of system malfunction.

## III. METHOD

The kinematic model of the cable-driven soft manipulator is based on the assumptions as follows:

- 1) The deformation of the continuum segment behaves as a circular arc [2].
- 2) The gravitational energy is negligible when compared to the elastic potential energy of each elastomer segment.
- 3) The disks are assumed to be infinitely thin so that the ends of each cable are perpendicular to the disks.
- 4) The cables are inextensible and remain in tension.

### A. Local Instantaneous Kinematics

For an  $n$ -segment continuum manipulator, the actuator space  $\mathbf{q}$  can be expressed by

$$\mathbf{q} = [\mathbf{q}_1 \quad \mathbf{q}_2 \quad \dots \quad \mathbf{q}_n]^T \in \mathbb{R}^{n \times 3} \quad (1)$$

and the actuator for the  $k$ th segment ( $k \leq n$ ) is

$$\mathbf{q}_k = [q_{k,1} \quad q_{k,2} \quad q_{k,3}]^T \in \mathbb{R}^3 \quad (2)$$

representing the actuation through three cables to realize a spatial motion for one segment. Under a small deformation, an  $n$ -segment continuum manipulator can be approximated by a finite set of consecutive constant curvatures [2], [36] geometrically in free space. The advantage of employing this geometric model is that it simplifies the infinite DOFs of each segment into a 2-DOF system—each inextensible segment ( $L_k$ ) can be bent on its own plane ( $\theta_k$ ), and a twist ( $\phi_k$ ) can be attained between the neighboring segments (see Fig. 3). For each segment, a twisting motion around its axial axis ( $\hat{\mathbf{z}}_k$ ) is neglected. The abovementioned description concludes the spatial configuration of the  $k$ th segment ( $\psi_k$ ) as  $\psi_k = [\theta_k \quad \phi_k]^T$  where we constrain  $\theta_k \in [0, \theta_{\max}]$  and  $\phi_k \in (-\pi, \pi]$ . Hence, the distal tip pose of each segment can be geometrically described. As illustrated in Fig. 3, we define a local Cartesian frame at the tip of each

segment following the right-hand rule, and set the axial axis as  $\hat{\mathbf{z}}_k$ . The analytic position of the  $k$ th segment w.r.t. its base (or the end-effector of the  $(k-1)$ th segment),  $\mathbf{p}_k^{k-1}$ , can be derived as

$$\mathbf{p}_k^{k-1} = \frac{L_k}{\theta_k} \begin{bmatrix} (1 - c_{\theta_k}) c_{\phi_k} \\ (1 - c_{\theta_k}) s_{\phi_k} \\ s_{\theta_k} \end{bmatrix} \quad (3)$$

where the notation  $c_{(\cdot)}$  and  $s_{(\cdot)}$  are the abbreviations for  $\cos(\cdot)$  and  $\sin(\cdot)$ , respectively.

The kinematics of the manipulator can be mapped through two relationships [26], namely the robot-specific mapping ( $f_{\text{spec}}$ ) and the robot-independent mapping ( $f_{\text{indp}}$ ) [2].

Noting that a numerical singularity will occur in (3) when there is no bending at the  $k$ th segment, viz.,  $\theta_k \rightarrow 0^+$ . Hence, Taylor series approximation was applied to (3) w.r.t. the bending angle of the  $k$ th segment ( $\theta_k$ ). To maintain high accuracy, a sixth-order Taylor polynomial was considered, and the approximation gives

$$\mathbf{p}_k^{k-1} = \begin{bmatrix} x_k^{k-1} \\ y_k^{k-1} \\ z_k^{k-1} \end{bmatrix} = L_k \begin{bmatrix} \frac{\theta_k c_{\phi_k} (\theta_k^4 - 30\theta_k^2 + 360)}{720} \\ \frac{\theta_k s_{\phi_k} (\theta_k^4 - 30\theta_k^2 + 360)}{720} \\ \frac{\theta_k^4 - 20\theta_k^2 + 120}{120} \end{bmatrix} \quad (4)$$

and the  $k$ th segment configuration ( $\psi_k$ ) can be derived as

$$\psi_k = \begin{bmatrix} \theta_k \\ \phi_k \end{bmatrix} = \begin{bmatrix} 2 \arccos \left( \frac{\|z_k^{k-1}\|}{\|\mathbf{p}_k^{k-1}\|_2} \right) \\ \arctan \left( \frac{y_k^{k-1}}{x_k^{k-1}} \right) \end{bmatrix} \quad (5)$$

where  $\|\cdot\|_2$  is the Euclidean norm.

For the cable-driven soft robot without a rotational base, at least three cables are required to teleoperate a single segment for spatial motion. By changing the length of the cables inside the elastomer, the soft segment can be bent toward the desired direction. Referring to the illustration and notation in Fig. 3, the relationship between the cable lengths and the configuration parameters can be geometrically derived as

$$L_{k,i} = L_k \underbrace{-\theta_k r c_{\phi_k + (i-1)\xi}}_{q_{k,i}} \quad (6)$$

where  $i \in \{1, 2, 3\}$  indicates the indexed cable  $A, B, C$ , and  $\xi = \frac{2\pi}{3}$  represents the trisection allocation between cables for one segment.  $\sum_{i=1}^3 L_{k,i} = 0$  holds in (6). The actuation of the  $i$ th cable can be concluded as the corresponding  $q_{k,i}$  for (2). The negative sign in  $q_{k,i}$  states the active pulling motion of the respective cable, while the opposite sign indicates a “pushing” motion. As described in Section II, our prototype follows a pulling-only mechanism, in which pushing a soft cable is not possible. To solve this problem, a pretensioning was applied to all cables, i.e., all cables were tightened at their rest state. In this context, a passive pushing motion was created by relaxing the cable to increase the cable length inside the elastomer. The

actuation velocity can be expressed by the infinitesimal step of  $\mathbf{q}_k$ , i.e.,  $\dot{\mathbf{q}}_k \approx \Delta \mathbf{q}_k$ . By taking the derivative of (6) w.r.t. the  $k$ th segment configuration  $\psi_k$ , the instantaneous kinematics can be derived as

$$\dot{\mathbf{q}}_k = \mathbf{J}_{kq\psi} \dot{\psi}_k \quad (7)$$

where

$$\mathbf{J}_{kq\psi} = \begin{bmatrix} -rc_{\phi_k} & r\theta_k s_{\phi_k} \\ -rc_{\phi_k + \xi} & r\theta_k s_{\phi_k + \xi} \\ -rc_{\phi_k + 2\xi} & r\theta_k s_{\phi_k + 2\xi} \end{bmatrix} \quad (8)$$

denotes the Jacobian matrix between the configuration and the actuation of the  $k$ th segment. The changing rate of the configuration can be approximated as its incremental change ( $\Delta$ ) of its corresponding positional change in the operational space

$$\dot{\mathbf{q}}_k = \mathbf{J}_{kq\psi} \Delta \psi_k = \mathbf{J}_{kq\psi} f_{\text{indp}}^{-1} (\Delta \mathbf{p}_k^{k-1}). \quad (9)$$

The  $k$ th segment configuration can be derived from the actuator space,  $\psi_k = f_{\text{spec}}(\mathbf{q}_k)$ , as

$$\theta_k(\mathbf{q}_k) = \frac{2\sqrt{q_{k,1}^2 + q_{k,2}^2 + q_{k,3}^2 - q_{k,1}q_{k,2} - q_{k,1}q_{k,3} - q_{k,2}q_{k,3}}}{3r} \quad (10)$$

$$\phi_k(\mathbf{q}_k) = \text{atan2} \left( 3(q_{k,2} - q_{k,3}), \sqrt{3}(q_{k,2} + q_{k,3} - 2q_{k,1}) \right) \quad (11)$$

where  $\text{atan2}(s_{\phi}, c_{\phi})$  computes the four-quadrant inverse tangent of  $s_{\phi}$  and  $c_{\phi}$  such that  $\phi \in (-\pi, \pi]$ .

As demonstrated in Fig. 3, the tip orientation of the  $k$ th segment w.r.t. its segmental base can be determined by three sequential rotations: rotating  $\phi_k$  around the  $\hat{\mathbf{z}}_{k-1}$  axis, then rotating  $\theta_k$  around the  $\hat{\mathbf{y}}_{k-1}$ , and finally rotating  $\phi_k$  reversely around the  $\hat{\mathbf{z}}_k$  axis of the current tip frame to ensure the nontwisting condition within each local segment [2]. Thus, the rotation matrix  $\mathbf{R}_k^{k-1}$  of the local segment is given by the following multiplication of rotation matrices as

$$\begin{aligned} \mathbf{R}_k^{k-1} &= \text{Rot}(\hat{\mathbf{z}}_{k-1}, \phi_k) \cdot \text{Rot}(\hat{\mathbf{y}}_{k-1}, \theta_k) \cdot \text{Rot}(\hat{\mathbf{z}}_k, -\phi_k) \\ &= \begin{bmatrix} c_{\phi_k}^2 c_{\theta_k} + s_{\phi_k}^2 & c_{\phi_k} s_{\phi_k} (c_{\theta_k} - 1) & c_{\phi_k} s_{\theta_k} \\ c_{\phi_k} s_{\phi_k} (c_{\theta_k} - 1) & s_{\phi_k}^2 c_{\theta_k} + c_{\phi_k}^2 & s_{\phi_k} s_{\theta_k} \\ -c_{\phi_k} s_{\theta_k} & -s_{\phi_k} s_{\theta_k} & c_{\theta_k} \end{bmatrix} \\ &\quad \underbrace{\quad}_{\mathbf{N}_k^{k-1}} \quad \underbrace{\quad}_{\mathbf{B}_k^{k-1}} \quad \underbrace{\quad}_{\mathbf{T}_k^{k-1}} \end{aligned} \quad (12)$$

where the operator  $\text{Rot}(\hat{\mathbf{u}}_k, \delta)$  represents a rotation matrix of rotating angle  $\delta$  along the unit axis  $\hat{\mathbf{u}}_k$ . The rotation matrix can be described in the form of three unit vectors of Frenet–Serret frame [2], as  $\mathbf{R}_k^{k-1} = [\mathbf{N}_k^{k-1} \quad \mathbf{B}_k^{k-1} \quad \mathbf{T}_k^{k-1}]$ , denoting the principal normal vector, binormal vector, and tangent vector of a frame attached to the distal tip of the  $k$ th segment. The angular velocity of the  $k$ th segment  $\omega_k^{k-1}$  is defined by the tangential motion of  $\mathbf{T}_k^{k-1}$ . It is known that [24]

$$\dot{\mathbf{T}}_k^{k-1} = \omega_k^{k-1} \times \mathbf{T}_k^{k-1} = [\omega_k^{k-1}]_{\times} \mathbf{T}_k^{k-1} \quad (13)$$



where  $[\cdot]_{\times}$  is the skew-symmetric operator, and  $\omega_k^{k-1} \cdot \mathbf{T}_k^{k-1} = 0$  since torsion is neglected. Based on the abovementioned, we can derive  $\omega_k^{k-1}$  by knowing  $\mathbf{T}_k^{k-1}$  through

$$\begin{aligned}\omega_k^{k-1} &= \omega_k^{k-1} \|\mathbf{T}_k^{k-1}\|^2 - \mathbf{T}_k^{k-1} (\mathbf{T}_k^{k-1} \cdot \omega_k^{k-1}) \\ &= [\mathbf{T}_k^{k-1}]_{\times} \left( [\omega_k^{k-1}]_{\times} \mathbf{T}_k^{k-1} \right).\end{aligned}\quad (14)$$

Substituting (13) into (14) produces the simplification of (14) as

$$\omega_k^{k-1} = [\mathbf{T}_k^{k-1}]_{\times} \dot{\mathbf{T}}_k^{k-1} \quad (15)$$

where  $[\mathbf{T}_k^{k-1}]_{\times}$  is the skew-symmetric matrix of  $\mathbf{T}_k^{k-1}$ , i.e.,

$$[\mathbf{T}_k^{k-1}]_{\times} = \begin{bmatrix} 0 & -c\theta_k & s\phi_k s\theta_k \\ c\theta_k & 0 & -c\phi_k s\theta_k \\ -s\phi_k s\theta_k & c\phi_k s\theta_k & 0 \end{bmatrix}. \quad (16)$$

Hence, the tip velocity of the  $k$ th segment can be derived by taking the derivative of (4) w.r.t. time, as

$$\mathbf{v}_k^{k-1} = \begin{cases} v_{k,x}^{k-1} = -\frac{L_k \theta_k^5 \dot{\phi}_k s\phi_k}{720} + \frac{L_k \theta_k^4 \dot{\theta}_k c\phi_k}{144} + \frac{L_k \theta_k^3 \dot{\phi}_k s\phi_k}{24} \\ v_{k,y}^{k-1} = \frac{L_k \theta_k^5 \dot{\phi}_k c\phi_k}{720} + \frac{L_k \theta_k^4 \dot{\theta}_k s\phi_k}{144} - \frac{L_k \theta_k^3 \dot{\phi}_k c\phi_k}{24} \\ v_{k,z}^{k-1} = \frac{L_k \theta_k^3 \dot{\theta}_k}{30} - \frac{L_k \theta_k \dot{\theta}_k}{3} \end{cases} \quad (17)$$

and the angular velocity can be derived from (15) as

$$\omega_k^{k-1} = \begin{bmatrix} -\dot{\theta}_k s\phi_k - \dot{\phi}_k c\phi_k c\theta_k s\theta_k \\ \dot{\theta}_k c\phi_k - \dot{\phi}_k c\theta_k s\phi_k s\theta_k \\ \dot{\phi}_k s\theta_k^2 \end{bmatrix}. \quad (18)$$

### B. Global Instantaneous Kinematics

Since each segment is simplified as a 2-DOF module based on the constant curvature assumption, a continuum manipulator with  $n$ -segment would have  $2n$  DOFs to be controlled. Assuming that a multisegment manipulator is homogeneous along the neighboring segments [24], for an  $n$ -segment robot, the tip frame pose of the  $k$ th segment ( $\Sigma_k$ ) w.r.t. the fixed base frame ( $\Sigma_0$ ), including the global position and orientation, can be recursively expressed by

$$\mathbf{p}_k^0 = \begin{cases} \mathbf{p}_k^{k-1}, & k = 1 \\ \mathbf{p}_{k-1}^0 + \mathbf{R}_{k-1}^0 \mathbf{p}_k^{k-1}, & k > 1 \end{cases} \quad (19)$$

and

$$\mathbf{R}_k^0 = \begin{cases} \mathbf{R}_k^{k-1}, & k = 1 \\ \mathbf{R}_{k-1}^0 \mathbf{R}_k^{k-1}, & k > 1. \end{cases} \quad (20)$$

The homogeneous transformation matrix of  $\Sigma_k$  w.r.t.  $\Sigma_0$  is

$$\mathbf{H}_k^0 = \begin{bmatrix} \mathbf{R}_k^0 & \mathbf{p}_k^0 \\ \mathbf{0}_{1 \times 3} & 1 \end{bmatrix} \in \text{SE}(3). \quad (21)$$

Moreover, the linear and angular velocity of the tip frame  $\Sigma_k$  w.r.t. the base frame  $\Sigma_0$  can be derived from the derivatives of

(19) and (20) as

$$\mathbf{v}_k^0 = \begin{cases} \mathbf{v}_k^{k-1}, & k = 1 \\ \dot{\mathbf{p}}_{k-1}^0 + (\dot{\mathbf{R}}_{k-1}^0 \mathbf{p}_k^{k-1} + \mathbf{R}_{k-1}^0 \mathbf{v}_k^{k-1}), & k > 1 \end{cases} \quad (22)$$

where  $\dot{\mathbf{R}}_{k-1}^0 = [\omega_{k-1}^0]_{\times} \mathbf{R}_{k-1}^0$ , and

$$\omega_k^0 = \begin{cases} \omega_k^{k-1}, & k = 1 \\ \omega_{k-1}^0 + \mathbf{R}_{k-1}^0 \omega_k^{k-1}, & k > 1. \end{cases} \quad (23)$$

### C. Verticalized-Tip Strategy for Suction

When using a suction tube to evacuate the salvaged blood from the surgical site, it is desired to have a continuous suction flow to minimize the air-blood exposure and the turbulent bubbling. Air contact during suction would have negative impacts (e.g., production of free hemoglobin [37] and leukocyte activation [38]) on the *in vitro* blood for future transfusion. From the safety perspective, it is preferable not to over insert the suction head into the fluid surface, as the negative pressure may harm the surrounding tissues. Therefore, the suction tip shall maintain a small distance under the liquid surface to ensure continuous suction. To prevent bubbling during the suction process, it would be preferable to keep the tip in a vertical pose while following the drop of the liquid level.

To comply with this unique sophistication, i.e., to maintain the suction tip in a vertical pose throughout the trajectory, we propose a configuration scheme to decouple the robot motion so that the orientation can be preserved while adjusting the tip to different positions. Several conditions should be fulfilled.

- 1) The instantaneous work plane is considered as a planar surface and initially, the tip can be set to be vertical and perpendicular to the work surface. The bending direction of the two segments is opposite to each other, i.e.,

$$\phi_2 = \phi_1 - \text{sgn}(\phi_1)\pi \quad (24)$$

where  $\phi_1 \in (-\pi, \pi]$ .

- 2) The distal tip is normal to the work surface, i.e.,

$$\theta_1 = \theta_2 \quad (25)$$

such that a special segment-associated configuration can be formed. This probing behavior ensures that the suction effectiveness and efficiency of the surgical tool.

- 3) The translational platform was calibrated to provide insertion-retraction motion, which is perpendicular to the work surface. It prevents the tip from neither drifting above the liquid nor touching the tissue surface to prevent fluid flow [39].

The RCM frame, as a spatially fixed frame, is given by inversely translating the proximal base frame along its  $\hat{\mathbf{z}}$ -axis. Hence, the new tip position becomes

$$\mathbf{p}_{\text{tip}}^{\text{RCM}} = \mathbf{p}_2^0 + \begin{bmatrix} 0 & 0 & h \end{bmatrix}^T \quad (26)$$

and  $z_2^0 + h = \epsilon$ , where  $\epsilon$  is a constant related to the definition of work surface w.r.t. the RCM, and  $h$  is the translation distance of the slide. In the case where the work surface is uneven or changing,  $\epsilon$  can be updated accordingly to match with the

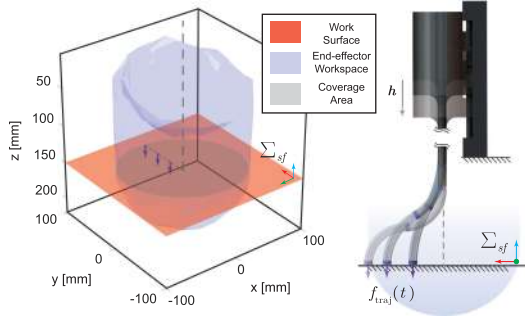


Fig. 4. Conceptual schematic of trajectory tracking of the verticalized-tip strategy: a two-segment continuum manipulator is mounted on an insertion platform, and the distal tip is tracking the desired trajectory  $f_{\text{traj}}(t)$  on the specific work surface.

condition of the work surface. By taking the derivative, the linear velocity of the new tip becomes  $\mathbf{v}_{\text{tip}}^{\text{RCM}} = \mathbf{v}_2^0 + [0 \ 0 \ \dot{h}]^T$ .

The additional translational DOF allows the tip to have a larger workspace, or, to maintain the tip pointing direction in certain work surfaces. This approach is often adopted in designing a robotic surgical tool [40]. The tip workspace of a two-segment soft continuum manipulator—with a total length of 100 mm, maximal segment bending angles of  $\frac{\pi}{2}$ , and maximal insertion depth of 80 mm—is shown in the schematic drawing of Fig. 4.

Adjusting different parameters within the allowable bending limit  $\theta_{\text{max}}$  enables the distal tip to operate on a large work surface. The twisting motion exhibited by the two neighboring segments should be opposite to each other, while degrees of bending of the two segments should be equal to minimize the orientation change in the tip. The motion through linear slide ( $h$ ) can be properly controlled to compensate any height change to achieve both planar and spatial trajectory task. Since  $h$  is restricted by  $\epsilon$  for the trajectory tracking task on specified surface, there is no null space of the robot tip. The opposite-bending configuration has also been adopted in [31] to reduce the DOFs of the task space from six (position + orientation) to only three (position).

#### D. Model Analysis and Simulation

The operating workspace and the performance of the robot were examined through simulation. The errors in position and velocity of the end-effector introduced by the Taylor series were examined and shown in Fig. S1 in the supplementary material. The errors are small and can be neglected.

When a blood region is detected, a suitable trajectory can be specified for the end-effector to perform the suction task. With the information from the image, the end-effector can be planned to move along or within the boundary of the blood region for cleaning and suctioning. To find the required actuator inputs for a given position, IK is needed. Unlike the work in [31] that employed a geometric approach to find the solution, this work considers searching the solution in a pregenerated point-cloud library based on the finite reachable 3-D position of the tip. First, the desired path defined on the work surface is required to send to the robotic system. However, the robot may not be capable of reaching every point on the desired path. Hence, a pseudotip path generator, as shown in Algorithm 1, was designed to compute the

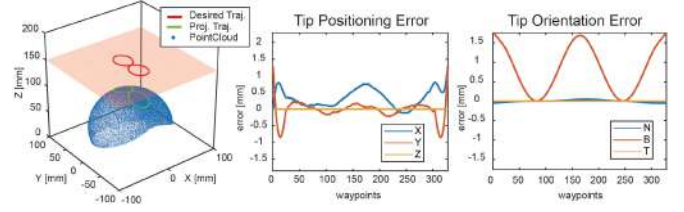


Fig. 5. Simulation performance of tip path planning.

#### Algorithm 1: Pseudo-Tip Path Generator.

---

**Input:**  $f_{\text{traj}} = \mathcal{P}_d \in \mathbb{R}^{3 \times m}$   
**Output:**  $\mathcal{P}_d^\dagger \in \mathbb{R}^{3 \times m}$ ,  $\mathbf{h} \in \mathbb{R}^{1 \times m}$

- 1 load  $3D\_pointCloud\_Lib$  as  $\mathcal{P}_{\text{lib}} \in \mathbb{R}^{3 \times 40000}$ ;
- 2  $\mathcal{P}_{\text{searchCenter}} := [\mathcal{P}_d(1, :), \mathcal{P}_d(2, :)]^T$ ;
- 3 **for**  $i \leftarrow 1, 2, \dots, m$  **do**
- 4    $\mathcal{P}_{\text{search}} \leftarrow |\mathcal{P}_{\text{lib}}(1 : 2, :) - \mathcal{P}_{\text{searchCenter}}(:, i)|$ ;
- 5    $[\sim, j] = \text{sort}(\|\mathcal{P}_{\text{search}}\|_2, \text{descend})$ ;
- 6    $\mathcal{P}_{\text{nearest}} := \mathcal{P}_{\text{lib}}(j(1), :, :)$ ;
- 7    $\mathcal{P}_d^\dagger(:, i) \leftarrow \mathcal{P}_{\text{nearest}}(:, j)$ ;
- 8  $\mathcal{P}_d^\dagger \leftarrow \text{smoothdata}(\mathcal{P}_d^\dagger, \text{sgolay})$ ;
- 9  $\mathbf{h} := \mathcal{P}_d(3, :) - \mathcal{P}_d^\dagger(3, :)$ ;
- 10 **save**  $\mathcal{P}_d^\dagger$  and  $\mathbf{h}$ ;

---

tip path for manipulator-only system. A 3-D point cloud data set (as shown in Fig. 5), noted as  $3D\_pointCloud\_Lib$  in Algorithm 1, with a size of 40 000 points in the form of Cartesian coordinate, was generated based on the two-segment manipulator's PCC parameters by varying the bending and twisting angles within the limit (see Section III-C) in advance. The number of 40 000 was empirically selected to balance the number of reachable points and the search speed. The kinematic-based point cloud can be generated in seconds.

In the pseudopath generator, the desired path, which was defined by  $m$  spatial points as  $\mathcal{P}_d \in \mathbb{R}^{3 \times m}$ , was first projected onto the spherical workspace, i.e., the 3-D point cloud, resulting in a curving pseudopath  $\mathcal{P}_d^\dagger$  of the manipulator itself. Then, a Savitzky–Golay filter was employed to smooth  $\mathcal{P}_d^\dagger$  by minimizing the least-square error by fitting a polynomial curve to the point cloud data. The required actuation to the manipulator can be inversely computed based on the pseudopath, which is defined in the manipulator base frame, and the insertion compensation can be obtained by subtracting the distance between  $\mathcal{P}_d$  and  $\mathcal{P}_d^\dagger$ . Examples of different planned trajectories and their respective polynomial on the 3-D point-cloud are shown in Fig. 5 and Fig. S2. With a smoothed pseudotip path and insertion compensation, a simulated tip path defined in  $\Sigma_{\text{RCM}}$  with proper tip orientation can be computed. Assuming that there is no physical coupling effect between segments, the simulated trajectory through the tip can be computed accordingly. Using a standard PC with an i7 CPU, the computational time from each given position to the cable actuation is around 1.25 ms. This approach can significantly reduce the computational time, enabling efficient real-time control.

The simulation results show that the tip can maintain the pointing direction in a vertical pose while following different desired paths in free space with a small positioning error. The error in simulation is mainly due to the simplification in the

approximated model to avoid the singularity. Besides, the projection bias on the point cloud data also contributes to the error. The actual tracking performances will be further demonstrated in Section IV.

### E. Controller Design

Considering the existence of the coupling effect between the segments, and the inherent material behaviors such as stiffness variation and material viscoelasticity, the soft continuum manipulator may not necessarily behave closely as predicted from the model. Hence, a visual feedback approach was employed to enhance the accuracy in tracking the spatial position of the end-effector. The position error of the segment tips  $e_p$  can be defined as the deviation of the current position vector  $p_c$  from the desired position vector  $p_d$  as

$$e_p = (p_d - p_c) \in \mathbb{R}^6. \quad (27)$$

The abovementioned error in the operational space can be independently mapped to the configuration space error [25] as

$$e_\psi = (\psi_d - \psi_c) \in \mathbb{R}^4. \quad (28)$$

Taking the time derivative of (28) and substituting by (9) gives

$$\dot{e}_\psi = \dot{\psi}_d - \lambda J_{q\psi}^\dagger \dot{q} \quad (29)$$

where  $\lambda$  denotes the positive scalar corresponding to the modeling uncertainties, the superscript  $\dagger$  is the left pseudoinverse, i.e.,  $J^\dagger = (JJ^\top)^{-1}J^\top$ , and  $\dot{q}$  is the actuation speed vector. The Jacobian is given by

$$J_{q\psi} = \underbrace{\begin{bmatrix} \mathbf{I} & \mathbf{I} \\ \mathbf{I} & \mathbf{0} \end{bmatrix}}_{\mathcal{A}} \begin{bmatrix} J_{1q\psi} & \mathbf{0} \\ \mathbf{0} & J_{2q\psi} \end{bmatrix} \in \mathbb{R}^{6 \times 4} \quad (30)$$

where  $\mathcal{A}$  represents the actuation coupling matrix between segments, and  $\mathbf{I} \in \mathbb{R}^{3 \times 3}$  is the identity matrix for the Jacobian coupling. The pose of the proximal segment shall be corrected together with the distal segment when the distal tip is changing its position through actuating the distal cables that running through the proximal segment. The control law is given by a linear proportional controller as

$$\dot{q} = J_{q\psi} (\dot{\psi}_d + K_P e_\psi) \quad (31)$$

where  $K_P$  is a symmetric positive definite matrix. It leads to the equivalent linear system as

$$\dot{e}_\psi + K_P e_\psi = \mathbf{0}. \quad (32)$$

The Lyapunov direct method can be utilized to determine a dependence  $\dot{q}(e_\psi)$  that ensures asymptotic stability of the system [41]. To show the asymptotic tracking, we consider the Lyapunov function candidate as follows:

$$V(e_\psi) = \frac{1}{2} e_\psi^\top K_P e_\psi \quad (33)$$

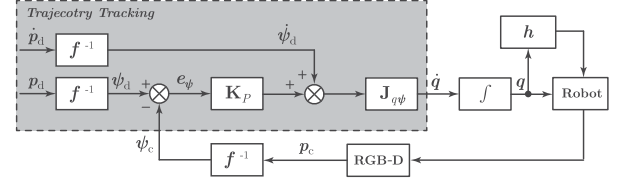


Fig. 6. Block scheme of the visual feedback controller for the soft robot.

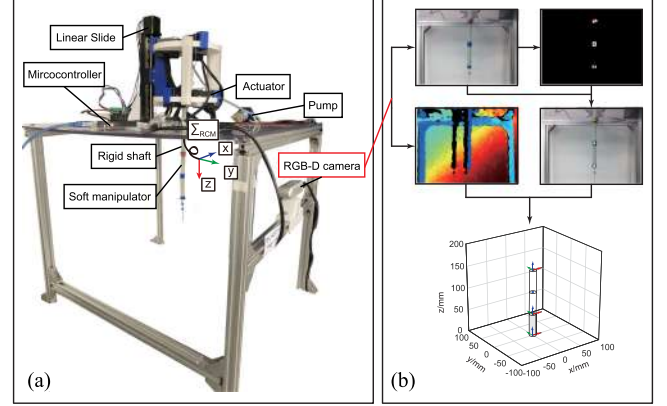


Fig. 7. (a) Experiment setup. (b) Image-based 3-D reconstruction.

such that  $V(e_\psi) > 0, \forall e_\psi \neq \mathbf{0}$ , and  $V(\mathbf{0}) = 0$ . Differentiating (33) w.r.t. time and accounting for (29) results in

$$\begin{aligned} \dot{V}(e_\psi) &= e_\psi^\top K_P \dot{e}_\psi \\ &= e_\psi^\top K_P \dot{\psi}_d - e_\psi^\top K_P \dot{\psi}_c \\ &= e_\psi^\top K_P \dot{\psi}_d - \lambda e_\psi^\top K_P J_{q\psi}^\dagger \dot{q} \\ &= e_\psi^\top K_P \dot{\psi}_d - \lambda e_\psi^\top K_P J_{q\psi}^\dagger J_{q\psi} (\dot{\psi}_d + K_P e_\psi). \end{aligned} \quad (34)$$

Under the assumption of a full rank Jacobian, it gives

$$\dot{V}(e_\psi) = (1 - \lambda) e_\psi^\top K_P \dot{\psi}_d - \lambda e_\psi^\top K_P K_P e_\psi. \quad (35)$$

If the desired tip position is reachable, consider the case of a constant reference as  $\dot{\psi}_d = \mathbf{0}$ , one gets:  $\dot{V}(e_\psi) = -\lambda e_\psi^\top K_P K_P e_\psi \leq 0$ , which implies that the function  $\dot{V}(e_\psi)$  is negative definite. By LaSalle theorem, it can be concluded that the system trajectory can uniformly converge to  $e_\psi = \mathbf{0}$ , i.e., the system is asymptotically stable. The convergence rate depends on the eigenvalues of matrix  $K_P$  and larger eigenvalues can lead to faster convergence. The tracking error  $e_\psi$  is norm-bounded: the larger the norm of  $K_P$ , the smaller the norm of  $e_\psi$ . The upper bound of the eigenvalues depends on the sampling time for a discrete-time system. The block diagram of the controller is shown in Fig. 6.

## IV. EXPERIMENTS

### A. Experiment Setup

The setup is given in Fig. 7(a), where the prototype is inversely mounted on a metal frame, with its tip pointing downward and

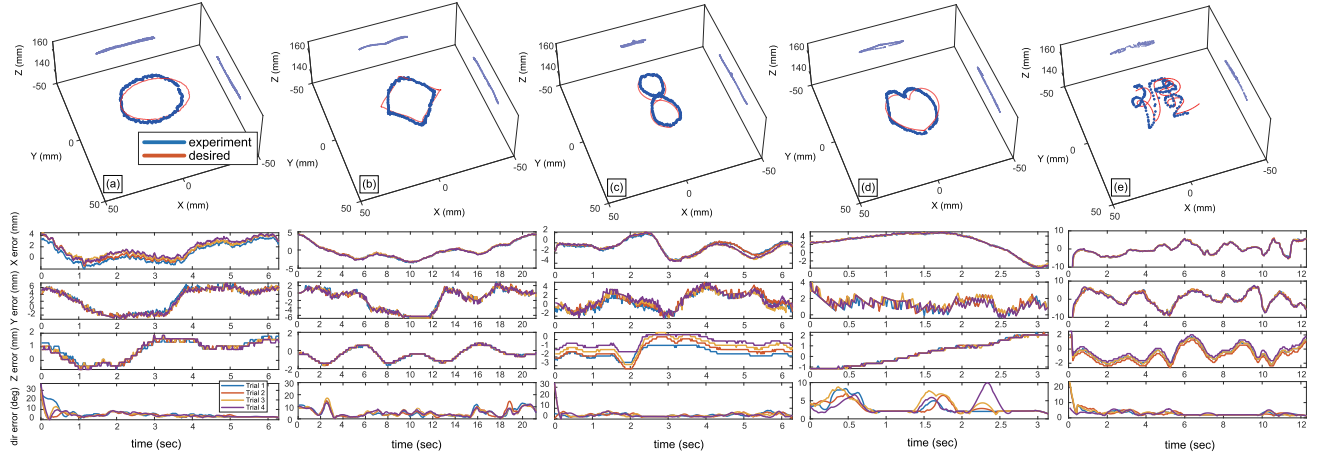


Fig. 8. Experiment on different trajectories of the robot tip at various speeds. (a) Oval. (b) Square. (c) Eight. (d) Heart. (e) Character “polytechnic.”

moving freely within the frame. The linear slide driven by a stepper motor was controlled via an Arduino board. An eye-to-hand system was used to monitor the spatial position and the velocity of the points-of-interest (POIs) labeled on the manipulator using an RGB-D camera (RealSense D435, Intel) to mimic the use of 3-D positioning systems, such as stereo-endoscope, EM tracking system, or ultrasound imaging system. In MIS (see Fig. 1), it is common to perform different surgical operations with the eye-to-hand configuration, where the endoscope is inserted from a separated trocar to monitor the surgical tools within the field of view [7], [35].

With proper camera calibration and noise filtering, the depth camera can capture the sequential image frames for evaluating the 3-D positions of the POIs. In this experiment, all the computations, visual sensing, and motors' control were run on MATLAB R2020a hosted by a PC with 16 GB RAM and i7-8th gen CPU. The image processing rate is at a steady 20 fps in 640×480p live stream, with a spatial positioning error within  $\pm 2.0$  mm after camera calibration. The origin of the world coordinate frame is set at the RCM point along the manipulator's rigid shaft which is 50 mm away from the base of the proximal segment [see Fig. 7(a)]. The coordinate of the manipulator's end-effector w.r.t. the RCM frame can be evaluated through homogeneous matrix transformation as  $\mathbf{H}_{\text{tip}}^{\text{RCM}} = (\mathbf{H}_{\text{RCM}}^{\text{cam}})^{-1} \cdot \mathbf{H}_{\text{tip}}^{\text{cam}}$ , where  $\mathbf{H}_{\text{RCM}}^{\text{cam}}$  is the homogeneous matrix of the spatial fixed RCM point expressed in the camera frame, and  $\mathbf{H}_{\text{tip}}^{\text{cam}}$  is the homogeneous matrix of the manipulator's tip expressed in the camera frame. These two terms can be obtained from the images. The workflow of image processing and 3-D coordinates computation is summarized in Fig. 7(b) and the supplementary text.

To measure the tip pointing direction, two additional blue markers were added to the distal tip. Hence, if there is an orientation change in the tip, the angle of the tip direction, intuitively represented as the angle deviated from the pointing normal, can be calculated from the images as  $\Theta = \text{atan2}(\|\mathbf{p}_{m,1}^{\text{RCM}} - \mathbf{p}_{m,2}^{\text{RCM}}\|_{xy}, \|\mathbf{p}_{m,1}^{\text{RCM}} - \mathbf{p}_{m,2}^{\text{RCM}}\|_z)$  where  $\|\mathbf{p}_A - \mathbf{p}_B\|$  denotes the distance between point  $A$  and  $B$  in the subscripted plane/axis expressed in  $\Sigma_{\text{RCM}}$ . In the experiment, we empirically set  $\lambda = 0.5$  and  $\mathbf{K}_P = \text{diag}(0.1, 0.1, 0.1, 0.1)$ .

TABLE I  
RMSE OF MEASURED TIP TRAJECTORIES IN FIG. 8

$N = 4$	RMSE				
	X (mm)	Y (mm)	Z (mm)	$\ \mathbf{p}\ _2$ (mm)	$\Theta$ ( $^\circ$ )
(a) oval	2.1100	4.1322	1.0510	4.7573	4.7722
(b) square	2.0456	3.0892	0.7800	3.7863	6.0377
(c) eight	1.5961	2.3500	1.2732	3.1130	3.7295
(d) heart	2.9796	2.4125	1.0374	3.9717	3.6361
(e) polytech	4.4080	4.7208	1.2079	6.5708	3.2493

## B. Results

The performance of positioning and orienting the tip to follow different trajectories can be evaluated by comparing the desired and measured values of  $\mathbf{p}_{\text{tip}}^{\text{RCM}}$  and  $\Theta$  from the built visual tracking system. The root-mean-square error (RMSE) of the tip is used to evaluate the position and angular deviation as  $\text{RMSE} = \sqrt{\frac{1}{N} \sum_{i=1}^N (\sum_{m=1}^m (\mathcal{V}_d - \mathcal{V}_c)^2)}$  where the desired value  $\mathcal{V}_d$  and camera-observed value  $\mathcal{V}_c$  are collected from  $N$  repeated trials of the same trajectory, and  $m$  denotes the number of nodes of a trajectory. As shown in Fig. 8, in our experiment, five different trajectories were examined, and each trajectory was repeated for 4 trials under the same condition without interfering the initial setting, such as the same starting position and the cable tension from the initial setup, to evaluate the repeatability of the system. The results are shown in Table I and Fig. 8.

The results indicate that the proposed verticalized-tip configuration strategy is capable of manipulating the two-segment soft robot to follow a desired trajectory in a designated work surface while keeping its tip in a vertical pose as much as possible. Under the given setting as specified, the maximum RMSE in positioning is less than 7 mm, while the angular offset is within  $6^\circ$ . The RMSE of tracking simple geometrical trajectories like in Table I(a)–(b) can be less than 5 mm. In addition, 3-D spiral trajectories mimicking continuous cleaning and suctioning in a circular motion were also examined. The related results are shown in the supplementary text.

The performance in tip positioning would also be influenced by the tip velocity, and thus, another set of experiments were conducted. As shown in Fig. 9, for a seven-point star, the trajectory involves the sharp and sudden motion changes at the



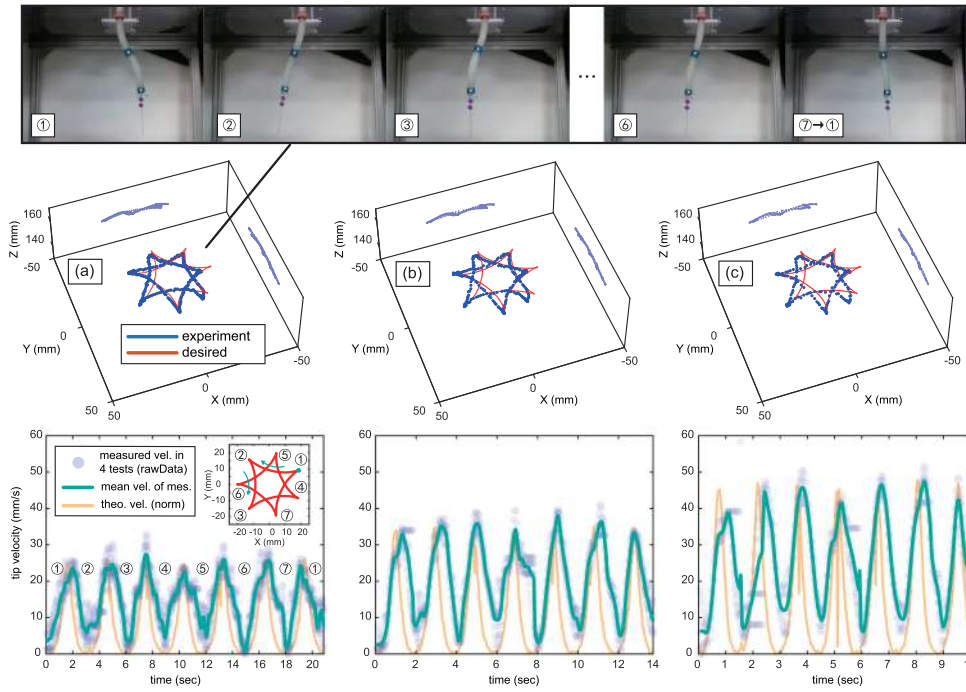


Fig. 9. Performance of different tip linear velocities in the same desired tip path: snapshots, 3-D view, and velocities.

TABLE II  
RMSE OF MEASURED TIP TRAJECTORIES IN FIG. 9

$N = 4$	RMSE			
	X (mm)	Y (mm)	Z (mm)	$\Theta$ ( $^\circ$ )
(a) $t=22.45s$ (20.85s)	2.9793	2.3642	1.0480	3.0382
(b) $t=14.95s$ (13.71s)	4.0386	3.3302	1.0107	3.6672
(c) $t=11.25s$ (10.20s)	4.6668	4.0376	1.0091	3.4044

The Brackets represent the mean of actual finished time.

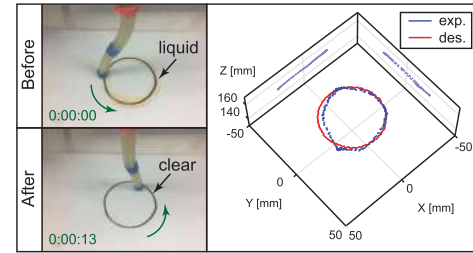


Fig. 10. Video screenshot: clearing the fluid on a circular trajectory.

corners. To define the velocity of the tip, the total time ( $t$ ) to complete the “drawing” of the whole path is required. For a given trajectory, a parametric function was used to output a set of key-points representing the desired path. Since the update rate of the controller is limited by the visual tracking system, which is at about 20 fps, the total time can be selected based on the number of key-points and its time interval. The seven-point star trajectory was completed under three different durations, and their RMSEs of the tip were averaged based on the four repeated trials. The results are shown in Table II.

It can be seen that the tip can finish drawing the trajectory faster than the desired time. The slight discrepancy is due to the controller with a faster update rate in actual practice. From the experiments, as the tip velocity increases, the RMSE in positioning changes from 3 mm to 5 mm, while the RMSE in orientation remains approximately  $3^\circ$ – $4^\circ$  at different speeds. The results show that the proposed scheme to verticalize the tip is robust to the tip velocity.

The suction performance of the robot while moving along the trajectory was examined. The robot was tested to remove liquid lying in a circular path. As shown in Fig. 10, the robot can follow along the path and remove the liquid efficiently.

### C. “Blood” Suction Automation

The performance of suction automation was examined. To mimic the surgical blood suction, a simple workflow, which includes the detection of the “bleeding” site, the automated planning of suction path, and the execution of suction, was designed. Similar to the laparoscopic setup of Fig. 1, a monocular camera was placed at the top as the endoscope to monitor and analyze the “blood” visually to generate a rounded zig-zag path that covers the bleeding site (see Fig. 11). Details of the image processing and path generation are summarized in Algorithm 2. A soft silicone container with uneven depth on each side was made to simulate the surgical site. A 12 V vacuum pump was connected to the base of the rigid shaft to provide continuous negative pressure for the tip. The robot was initially configured with its tip slightly and vertically dipped into the liquid surface to ensure a continuous suction.

As the suction proceeds, the level of the liquid surface would decrease over time. Based on the image-based estimation on the area of the blood region and the suction efficiency (approx.

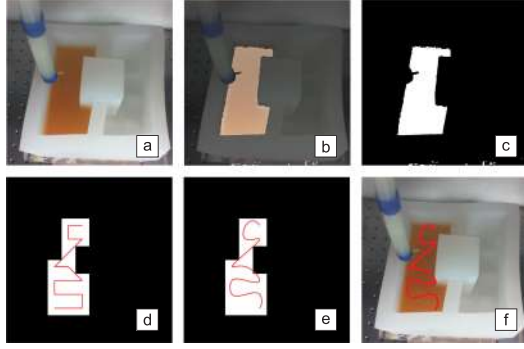


Fig. 11. Path planning for suction. (a) RGB image. (b) Color-based segmentation. (c) Binarized image. (d) Pixelized image with zig-zag path. (e) Spline interpolation. (f) Upshot.

#### Algorithm 2: Suction Path Generator.

**Input:** RGB image  $C$ , desired pixel resolution  $U, V$   
**Result:** Suction path as  $P_{\Delta}^{\text{RCM}}$

- 1 Import image as  $C$ ;
- 2 Subtract damped red  $r$  from  $\text{rgb2gray}(C)$  as  $C_r$ ;
- 3 Binarize and dilate  $C_r$  as  $C_{br}$ ;
- 4 Pixelize  $C_{br}$  as  $C_{br}^* \in \mathbb{R}^{U \times V}$ ;
- 5 for  $i = 1 : U$  do
- 6     if  $\text{mod}(i, 2) == 1$  then
- 7         for  $j = 1 : 1 : V$  do
- 8             if  $C_{br}^*(i, j) == 1$  then
- 9                  $P \leftarrow [P, [j, i]]^T$ ;
- 10         else
- 11             for  $j = V : -1 : 1$  do
- 12                 if  $C_{br}^*(i, j) == 1$  then
- 13                      $P \leftarrow [P, [j, i]]^T$ ;
- 14     Connect the centered coordinates in  $P$  as line  $P_{\Delta}$ ;
- 15     Smooth  $P_{\Delta} \leftarrow \text{interp1}(P_{\Delta}, \text{spline})$ ;
- 16     Align  $P_{\Delta}$  with  $H_{\text{tip}}^{\text{RCM}}$  and assign to the robot as  $P_{\Delta}^{\text{RCM}}$ ;

80 mL/min), the additional motion required on the linear slide to maintain the tip to the surface can be computed accordingly. The performance of the automated suction process is shown in Fig. 12 and the supplementary videos, and the results confirm that the generated path can guide the soft robotic tool to remove blood in the environment.

#### D. Discussion

The performance of the tracking could be influenced by a number of factors, such as the system assembly and the cable tension. Also, the tracking system contributes to the errors in measuring the tip. Systematic errors are introduced by the PCC model without the consideration of material contraction, the projected trajectories onto the randomly generated point cloud as a workspace, and Taylor approximation on the tip pose. However, since each segment is limited to a bend with less than  $90^\circ$ , the axial contraction is not significant and the constant curvature simplification holds.

As shown in Table III, a brief comparison of the tip trajectory tracking performance (in RMSE) among other similar surgical-size soft robotic manipulators in free space is provided. We consider a manipulator with a diameter less than 20 mm would

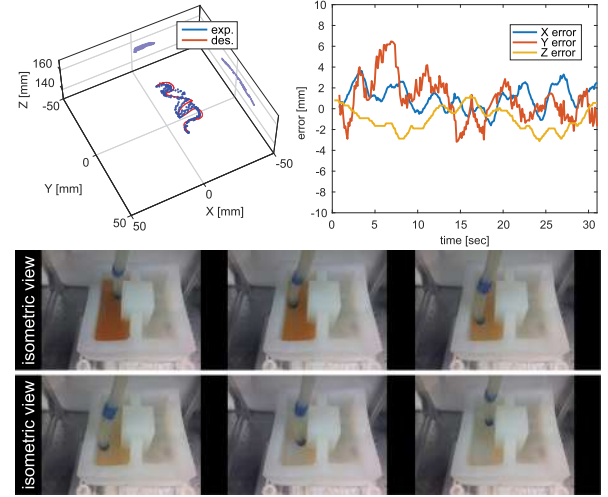


Fig. 12. Automated “blood” suction based on the image-based auto-generated trajectory using the proposed soft robotic suction tool.

TABLE III  
COMPARISON: RMSE OF TIP TRAJECTORY TRACKING OF OTHER SIMILAR SURGICAL-SIZE SOFT MANIPULATORS IN FREE SPACE

Ref.	$\varnothing$ (mm)	len. of seg. (mm)	#seg.	RMSE
[9]	13	93	1	2–8°
[16]	19	95	1	<30 pixels
[18]	13	67	1	<17 pixels
[42]	27	70	2	<11 mm
[23]	14.5	50	2	4–6°/segment
ours	9	50	2	<7 mm

be suitable for the MIS purpose, as the size of incisions is usually ranged 5–15 mm [8] in a laparoscopic intervention. Some prototypes are interested in single-segment soft manipulator [9], [16], [18], which allow a 2-DOF (bending and bending direction) tracking. Model-free approaches were considered in [9], [16], [18], and [42], and different sensing techniques, such as FBG, EM sensor, eye-in-hand visual servoing, were utilized for tool tracking. These works demonstrate satisfactory performances in tracking the tip in free space, and they are comparable to our method based on kinematic modeling without the need for extensive data training or expensive sensors.

Comparing our soft robotic tool with conventional suction tools, there are several advantages, including, (i) less damage to the surrounding tissue; and (ii) a vertical tip pose to improve effectiveness and to reduce the undesired bubbling effect. Experiments were conducted to showcase the abovementioned claims. As shown in Fig. 13, a rigid tool has limited dexterity when operating in a constrained environment. Since the tool is also constrained by the RCM, the angle of the tip is kept changing and the tip is unable to maintain in a vertical pose throughout the trajectory. Besides, it was difficult to manipulate the tool to reach different locations. Some regions could be hard to reach and the fluid could not be removed. In addition, with limited dexterity, the tool could easily exert undesired force to the surrounding, causing potential damage to the environment. Although a replicated suction tip can be added to the rigid tool to provide extra flexibility to adjust the tip angle at the very distal end (see Fig. 14), the problems on the reachability and the

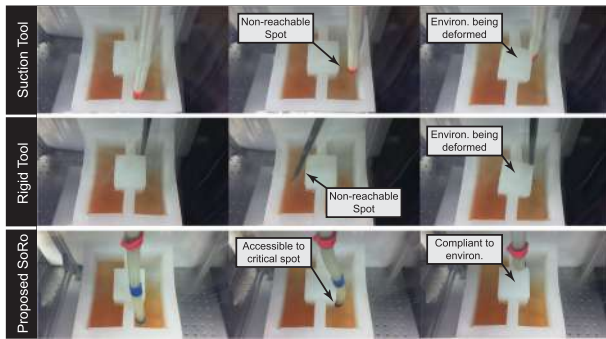


Fig. 13. Comparison of the replicated bendable suction tool, the rigid surgical tool, and the proposed soft continuum robot.



Fig. 14. Tip of a suction tool (Image: Intuitive Surgical, Inc.); CAD replica of the tip; 3D-printed rigid suction tool (PLA, NiTi wires, and interior hose).

undesired force to the surrounding could still exist. In contrast, those problems can be solved with our soft robotic tool and a continuous suction can be achieved.

In this article, there are several limitations as compared to the a real laparoscopic surgery. First, the tip can be tracked in an open and wide view throughout the experiment, but it could be blocked or occluded during the surgery. Therefore, position estimation algorithms, such as Kalman filters, could be added to improve the robustness. Second, the field of view from the endoscopic is limited, and image stitching techniques could be employed to enlarge the view for different operations.

## V. CONCLUSION

In this article, we introduce a disposable cable-driven soft-bodied continuum manipulator as a robotic suction tool for laparoscopic surgeries. An opposite-bending configuration scheme for the soft manipulator was adopted, ensuring the pointing direction of the robot tip to be perpendicular to the working surface while performing a free-space tip trajectory tracking task. Based on a search-based IK solver, a simulation was performed to validate the performance and the tip can keep in a vertical pose with a positioning error of less than 2.5 mm in different paths. A 3-D visual feedback system using RGB-D images was built, which can be used to enhance the accuracy with kinematic control. Experiment results confirm the feasibility of the proposed verticalized-tip scheme method to follow different trajectories, with an RMSE of less than 7 mm in position and within 6° in orientation. Different experiments were also conducted to evaluate the performance of automated suction. Comparison with existing work on soft robot control was studied, and our method can achieve similar performance in keeping the positioning accuracy along the trajectory, and at the same time, enabling the tip in a vertical pose to perform

the suctioning. An automated suction procedure was designed and performed. A comparison between the soft surgical tool and rigid tools was given, showing that the latter were outweighed by the former in terms of interaction safety, reachable workspace, and vertical tip configuration.

## ACKNOWLEDGMENT

The authors would like to deeply thank the anonymous reviewers for their precious comments that have significantly improved the completeness and quality of this article.

## REFERENCES

- [1] D. Rus and M. T. Tolley, "Design, fabrication and control of soft robots," *Nature*, vol. 521, no. 7553, pp. 467–475, 2015.
- [2] R. J. Webster III and B. A. Jones, "Design and kinematic modeling of constant curvature continuum robots: A review," *Int. J. Robot. Res.*, vol. 29, no. 13, pp. 1661–1683, 2010.
- [3] L. Zhang *et al.*, "Prevention and management of hemorrhage during a laparoscopic colorectal surgery," *Ann. Laparoscopic Endoscopic Surg.*, vol. 1, no. 7, pp. 269–274, 2016.
- [4] J. Burgner-Kahrs, D. C. Rucker, and H. Choset, "Continuum robots for medical applications: A survey," *IEEE Trans. Robot.*, vol. 31, no. 6, pp. 1261–1280, Dec. 2015.
- [5] B. Lu, H. K. Chu, K. Huang, and L. Cheng, "Vision-based surgical suture looping through trajectory planning for wound suturing," *IEEE Trans. Autom. Sci. Eng.*, vol. 16, no. 2, pp. 542–556, Apr. 2019.
- [6] D. Navarro-Alarcon *et al.*, "Developing a compact robotic needle driver for MRI-guided breast biopsy in tight environments," *IEEE Robot. Autom. Lett.*, vol. 2, no. 3, pp. 1648–1655, Jul. 2017.
- [7] Y. Fong, Y. Woo, W. J. Hyung, C. Lau, and V. E. Strong, *The SAGES Atlas of Robotic Surgery*. Berlin, Germany: Springer, 2018.
- [8] D. Bhandarkar, G. Mittal, R. Shah, A. Katara, and T. E. Udawadia, "Single-incision laparoscopic cholecystectomy: How i do it?" *J. Minimal Access Surg.*, vol. 7, no. 1, pp. 17–23, 2011.
- [9] K.-H. Lee *et al.*, "Nonparametric online learning control for soft continuum robot: An enabling technique for effective endoscopic navigation," *Soft Robot.*, vol. 4, no. 4, pp. 324–337, 2017.
- [10] M. Girelli, F. Renda, M. Calisti, A. Arienti, G. Ferri, and C. Laschi, "Neural network and Jacobian method for solving the inverse statics of a cable-driven soft arm with nonconstant curvature," *IEEE Trans. Robot.*, vol. 31, no. 4, pp. 823–834, Aug. 2015.
- [11] J. Lai, K. Huang, and H. K. Chu, "A learning-based inverse kinematics solver for a multi-segment continuum robot in robot-independent mapping," in *Proc. IEEE Int. Conf. Robot. Biomimetics*, 2019, pp. 576–582.
- [12] P. Hyatt, D. Wingate, and M. D. Killpack, "Model-based control of soft actuators using learned non-linear discrete-time models," *Front. Robot. AI*, vol. 6, p. 22, 2019.
- [13] T. G. Thuruthel, B. Shih, C. Laschi, and M. T. Tolley, "Soft robot perception using embedded soft sensors and recurrent neural networks," *Sci. Robot.*, vol. 4, no. 26, 2019, Art. no. eaav1488.
- [14] K. Elgenciy, N. Lohse, and M. Jackson, "Bending angle prediction and control of soft pneumatic actuators with embedded flex sensors—a data-driven approach," *Mechatronics*, vol. 50, pp. 234–247, 2018.
- [15] M. C. Yip and D. B. Camarillo, "Model-less feedback control of continuum manipulators in constrained environments," *IEEE Trans. Robot.*, vol. 30, no. 4, pp. 880–889, Aug. 2014.
- [16] X. Wang *et al.*, "Eye-in-hand visual servoing enhanced with sparse strain measurement for soft continuum robots," *IEEE Robot. Autom. Lett.*, vol. 5, no. 2, pp. 2161–2168, Apr. 2020.
- [17] H. Wang, B. Yang, Y. Liu, W. Chen, X. Liang, and R. Pfeifer, "Visual servoing of soft robot manipulator in constrained environments with an adaptive controller," *IEEE/ASME Trans. Mechatron.*, vol. 22, no. 1, pp. 41–50, Feb. 2017.
- [18] G. Fang *et al.*, "Vision-based online learning kinematic control for soft robots using local Gaussian process regression," *IEEE Robot. Autom. Lett.*, vol. 4, no. 2, pp. 1194–1201, Apr. 2019.
- [19] F. Xu, H. Wang, J. Wang, K. W. S. Au, and W. Chen, "Underwater dynamic visual servoing for a soft robot arm with online distortion correction," *IEEE/ASME Trans. Mechatron.*, vol. 24, no. 3, pp. 979–989, Jun. 2019.



- [20] M. Benosman, F. Boyer, G. Le Vey, and D. Primault, "Flexible links manipulators: From modelling to control," *J. Intell. Robot. Syst.*, vol. 34, no. 4, pp. 381–414, 2002.
- [21] T. Kato, I. Okumura, S.-E. Song, A. J. Golby, and N. Hata, "Tendon-driven continuum robot for endoscopic surgery: Preclinical development and validation of a tension propagation model," *IEEE/ASME Trans. Mechatron.*, vol. 20, no. 5, pp. 2252–2263, Oct. 2015.
- [22] F. Renda, M. Cianchetti, M. Giorelli, A. Arienti, and C. Laschi, "A 3D steady-state model of a tendon-driven continuum soft manipulator inspired by the octopus arm," *Bioinspiration Biomimetics*, vol. 7, no. 2, 2012, Art. no. 025006.
- [23] H. Abidi *et al.*, "Highly dexterous 2-module soft robot for intra-organ navigation in minimally invasive surgery," *Int. J. Med. Robot. Comput. Assist. Surg.*, vol. 14, no. 1, 2018, Art. no. e1875.
- [24] W. S. Rone and P. Ben-Tzvi, "Continuum robot dynamics utilizing the principle of virtual power," *IEEE Trans. Robot.*, vol. 30, no. 1, pp. 275–287, Feb. 2014.
- [25] A. Bajo, R. E. Goldman, and N. Simaan, "Configuration and joint feedback for enhanced performance of multi-segment continuum robots," in *Proc. IEEE Int. Conf. Robot. Autom.*, 2011, pp. 2905–2912.
- [26] B. A. Jones and I. D. Walker, "Kinematics for multisection continuum robots," *IEEE Trans. Robot.*, vol. 22, no. 1, pp. 43–55, Feb. 2006.
- [27] C. Della Santina, A. Bicchi, and D. Rus, "On an improved state parametrization for soft robots with piecewise constant curvature and its use in model based control," *IEEE Robot. Autom. Lett.*, vol. 5, no. 2, pp. 1001–1008, Apr. 2020.
- [28] J. Lai, B. Lu, and H. K. Chu, "Variable-stiffness control of a dual-segment soft robot using depth vision," *IEEE/ASME Trans. Mechatron.*, to be published. doi: [10.1109/TMECH.2021.3078466](https://doi.org/10.1109/TMECH.2021.3078466).
- [29] P. Qi, C. Liu, A. Ataka, H.-K. Lam, and K. Althoefer, "Kinematic control of continuum manipulators using a fuzzy-model-based approach," *IEEE Trans. Ind. Electron.*, vol. 63, no. 8, pp. 5022–5035, Aug. 2016.
- [30] G. Gerboni, A. Diodato, G. Ciuti, M. Cianchetti, and A. Menciassi, "Feedback control of soft robot actuators via commercial flex bend sensors," *IEEE/ASME Trans. Mechatronics*, vol. 22, no. 4, pp. 1881–1888, Aug. 2017.
- [31] Z. Gong *et al.*, "A soft manipulator for efficient delicate grasping in shallow water: Modeling, control, and real-world experiments," *Int. J. Robot. Res.*, vol. 40, pp. 449–469, 2020.
- [32] S. Neppalli, M. A. Csencsits, B. A. Jones, and I. D. Walker, "Closed-form inverse kinematics for continuum manipulators," *Adv. Robot.*, vol. 23, no. 15, pp. 2077–2091, 2009.
- [33] E. Coevoet *et al.*, "Software toolkit for modeling, simulation, and control of soft robots," *Adv. Robot.*, vol. 31, no. 22, pp. 1208–1224, 2017.
- [34] J. Lai, K. Huang, B. Lu, and H. K. Chu, "Toward vision-based adaptive configuring of a bidirectional two-segment soft continuum manipulator," in *Proc. IEEE/ASME Int. Conf. Adv. Intell. Mechatronics*, 2020, pp. 934–939.
- [35] C.-H. Kuo and J. S. Dai, "Robotics for minimally invasive surgery: A historical review from the perspective of kinematics," in *Proc. Int. Symp. Hist. Mach. Mech.*, 2009, pp. 337–354.
- [36] I. A. Gravagne, C. D. Rahn, and I. D. Walker, "Large deflection dynamics and control for planar continuum robots," *IEEE/ASME Trans. Mechatronics*, vol. 8, no. 2, pp. 299–307, Jun. 2003.
- [37] S.-B. An, E. S. Choi, and W. Ahn, "Suction conditions for minimizing the production of free hemoglobin during blood salvage using an autotransfusion apparatus," *Korean J. Anesthesiol.*, vol. 60, no. 4, pp. 266–271, 2011.
- [38] A. M. El-Sabbagh, C. J. Toomasian, J. M. Toomasian, G. Ulysse, T. Major, and R. H. Bartlett, "The effect of air exposure and suction on blood cell activation & hemolysis in an in-vitro cardiomy suction model," *Asaio J.*, vol. 59, no. 5, pp. 474–479, 2013.
- [39] F. Richter *et al.*, "Autonomous robotic suction to clear the surgical field for hemostasis using image-based blood flow detection," *IEEE Robot. Autom. Lett.*, vol. 6, no. 2, pp. 1383–1390, Apr. 2021.
- [40] J. Ding, R. E. Goldman, K. Xu, P. K. Allen, D. L. Fowler, and N. Simaan, "Design and coordination kinematics of an insertable robotic effectors platform for single-port access surgery," *IEEE/ASME Trans. Mechatronics*, vol. 18, no. 5, pp. 1612–1624, Oct. 2012.
- [41] B. Siciliano, L. Sciacivico, L. Villani, and G. Oriolo, *Robotics: Modelling, Planning and Control*. Berlin, Germany: Springer, 2010.
- [42] J. D. Ho *et al.*, "Localized online learning-based control of a soft redundant manipulator under variable loading," *Adv. Robot.*, vol. 32, no. 21, pp. 1168–1183, 2018.



**Jiewen Lai** (Student Member, IEEE) received the B.Eng. degree in metallurgical engineering from the Wuhan University of Science and Technology, Wuhan, China, in 2016, and the M.Sc. degree in mechanical and automation engineering from The Chinese University of Hong Kong (CUHK), Hong Kong, in 2017. He is currently working toward the Ph.D. degree in mechanical engineering with The Hong Kong Polytechnic University, Hong Kong.

His research interests include soft/continuum robots, surgical robots, and robot intelligence.



**Kaicheng Huang** received the B.Eng. degree in automation from Shenzhen University, Shenzhen, China, in 2014, and the M.Sc. degree in mechanical and automation engineering from The Chinese University of Hong Kong, Hong Kong, in 2015, and the Ph.D. degree in mechanical engineering from the Department of Mechanical Engineering, The Hong Kong Polytechnic University, Hong Kong, in 2020.

He was a Postdoctoral Fellow with the University of Hong Kong (HKU), Hong Kong, from 2020 to 2021. He is currently a Postdoctoral Fellow with Southern University of Technology (SUSTech), Shenzhen, China. His research interests include automated cell patterning, robotic control, and machine learning.



**Bo Lu** received the B.Eng. degree in ship and offshore engineering from the Dalian University of Technology, Dalian, China, in 2013, and the M.S. and Ph.D. degrees from The Hong Kong Polytechnic University, Hong Kong, in 2015 and 2019, respectively, both in mechanical engineering.

He has been a Postdoctoral Research Fellow with the T Stone Robotics Institute, The Chinese University of Hong Kong (CUHK), Hong Kong, since 2019. He will be joining the School of Mechanical and Electrical Engineering, Soochow University, Suzhou, China, as an Associate Professor, in late 2021. His current research interests include medical robotics, computer vision, and surgical automation technique.



**Qingxiang Zhao** received the B.Eng. and M.S. degrees from Sichuan University, Chengdu, China, in 2016 and 2019, respectively, both in mechanical engineering. He is currently working toward the Ph.D. degree in mechanical engineering with The Hong Kong Polytechnic University, Hong Kong.

His research interests include soft robotics, industrial automation, and artificial intelligence.



**Henry K. Chu** (Member, IEEE) received the B.S. degree in mechanical engineering from the University of Waterloo, Waterloo, ON, Canada, in 2005, and the M.A.Sc. and Ph.D. degrees in mechanical and industrial engineering from the University of Toronto, Toronto, ON, in 2007 and 2011, respectively.

He was a Postdoctoral Fellow with the University of Toronto, Toronto, ON, Canada, and the City University of Hong Kong, Hong Kong. He is currently an Assistant Professor with The Hong Kong Polytechnic University, Hong Kong. His research interests include robotic manipulation, vision-based control and automation, microsystem design, and tissue engineering.

Dr. Chu was the recipient of the top-ranked Canada Graduate Scholarship (CGS) (2009–2011) and the preapproved candidate of the Industrial R&D Fellowships (IRDF) Program (2012) from the Natural Sciences and Engineering Research Council of Canada (NSERC).